Energy Storage Materials 14 (2018) 169–178

Contents lists available at ScienceDirect

Energy Storage Materials

journal homepage: www.elsevier.com/locate/ensm

High-rate, long cycle-life Li-ion battery anodes enabled by ultrasmall tin-based nanoparticles encapsulation

Wei Ai[a,b,c], Zhennan Huang[d], Lishu Wu[b], Zhuzhu Du[c], Chenji Zou[b], Ziyang He[e], Reza Shahbazian-Yassar[d], Wei Huang[a,c,f,*], Ting Yu[b,**]

[a] Shaanxi Institute of Flexible Electronics (SIFE), Northwestern Polytechnical University (NPU), 127 West Youyi Road, Xi'an 710072, China
[b] Division of Physics and Applied Physics, School of Physical and Mathematical Sciences, Nanyang Technological University, 637371 Singapore, Singapore
[c] Key Laboratory of Flexible Electronics (KLOFE) & Institute of Advanced Materials (IAM), Jiangsu National Synergetic Innovation Center for Advanced Materials (SICAM), Nanjing Tech University (NanjingTech), 30 South Puzhu Road, Nanjing 211816, China
[d] Department of Mechanical and Industrial Engineering, University of Illinois at Chicago, Chicago, IL 60607, United States
[e] Department of Economics, Columbia University, New York, NY 10027, United States
[f] Key Laboratory for Organic Electronics & Information Displays (KLOEID) and Institute of Advanced Materials (IAM), SICAM, Nanjing University of Posts & Telecommunications, Nanjing 210023, Jiangsu, China

ARTICLE INFO

Keywords:
Sn-based nanoparticles
Graphene
Hierarchically porous carbon
Li-ion batteries
Long-term cyclability

ABSTRACT

Tin (Sn)-based materials are potential alternatives to the commercial graphite anode for next generation Li-ion batteries, but their successful application is always impeded by fast capacity fading upon cycling that stemmed from huge volume variations during lithiation and delithiation. We develop an applicable strategy of encapsulating sub-10-nm-sized Sn-based nanoparticles (i.e., Sn and SnO_2) in nitrogen/phosphorus codoped hierarchically porous carbon (NPHPC) or NPHPC-reduced graphene oxide hybrid (NPHPC-G) to effectively solve the issues of Sn-based anodes. Benefiting from the peculiar structure, the composites exhibit unprecedented electrochemical behaviors, for example, NPHPC-G@Sn and NPHPC-G@SnO_2 deliver a high reversible capacity of ~1158 and ~1366 mAh g^{-1} at 200 mA g^{-1}, respectively, and maintain at ~1099 mAh g^{-1} after 500 cycles and ~1117 mAh g^{-1} after 300 cycles. *In situ* transmission electron microscopy and *ex situ* scanning electron microscopy observations unveil that these composites are able to withstand the volume changes of Sn-based nanoparticles while sustaining the framework of the architectures and hence conferring outstanding electrochemical properties. Our present work provides both *in situ* and *ex situ* techniques for understanding the so-called synergistic effect between metals or metal oxides and carbons, which may offer rational guidance to design carbon-based functional materials for energy storage.

1. Introduction

Li-ion batteries (LIBs), the currently predominate power source for portable electronics, have been considered as the most promising clean energy technology for the booming electric vehicles and stationary energy storage [1,2]. However, conventional LIBs based on insertion-compound materials (i.e., graphite anodes and lithium transition metal oxide or phosphate cathodes) are approaching their intrinsic limit of specific energy (~210 Wh kg^{-1}), which cannot satisfy the ever-growing demand for energy [3–6]. A further increase in charge storage capability of LIBs requires an increase in the specific capacity of the electrode materials. Tin (Sn)-based materials, with high theoretical specific capacity [e.g., ~990 mAh g^{-1} for Sn, ~780 mAh g^{-1} (considering only the reversible alloying reaction) for SnO_2] and low discharge potential versus Li/Li^+, are potentially feasible alternatives to the conventional graphite anodes for next generation of LIBs [7,8]. Since Fujifilm Celltec Company initially announced the commercialization of Sn-based amorphous composite oxide as a negative electrode in 1997 [9], a great deal of research efforts have been devoted to developing advanced Sn-based anodes. Yet the practical implementation of Sn-based anodes faces the insurmountable challenges of huge volume variations [10,11], for example, ~260% for Sn and ~300% for SnO_2, during the alloying and dealloying, resulting in poor cyclability stemming from the pulverization of electrodes associated with the parasitic phenomena (i.e., continuous formation of solid electrolyte interphase (SEI) and electrical disconnection with the current collector).

* Corresponding author at: Division of Physics and Applied Physics, School of Physical and Mathematical Sciences, Nanyang Technological University, 637371 Singapore, Singapore.
** Corresponding author.
E-mail addresses: iamwhuang@nwpu.edu.cn (W. Huang), yuting@ntu.edu.sg (T. Yu).

https://doi.org/10.1016/j.ensm.2018.02.008
Received 5 February 2018; Accepted 8 February 2018
Available online 01 March 2018
2405-8297/

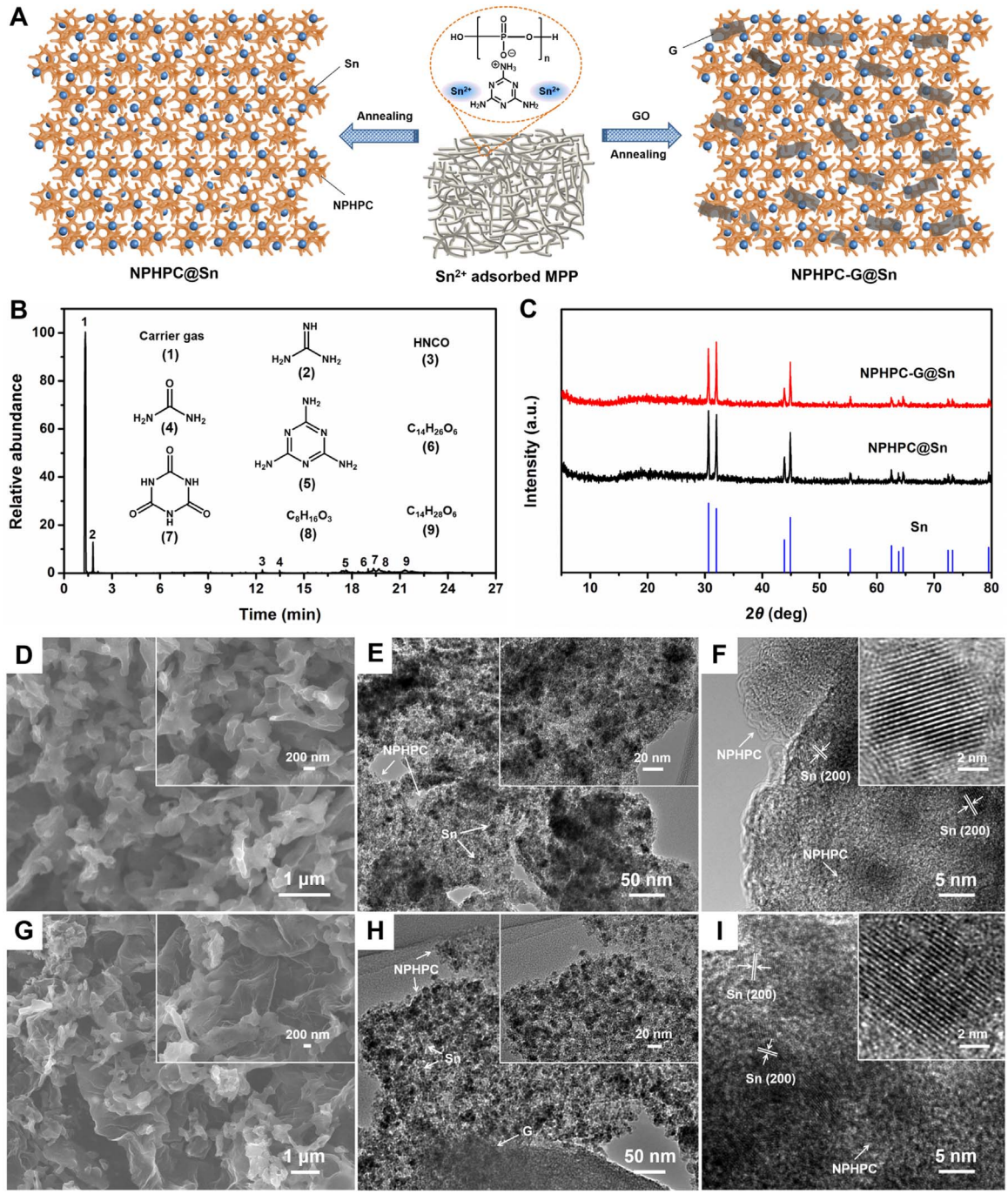

Fig. 1. Schematic diagrams of fabrication and characterizations of the NPHPC@Sn and NPHPC-G@Sn. (A) Schematic illustration of the fabrication procedures of NPHPC@Sn and NPHPC-G@Sn by *in situ* carbonization of Sn^{2+} absorbed MPP. GO is introduced as the precursor of graphene towards the fabrication of NPHPC-G@Sn. (B) Py-GC/MS chromatogram obtained upon heating MPP to 700 °C for 30 s. The numbers represent the major pyrolysis products of MPP, wherein 1, the predominant peak, stems from the carrier gas, helium. (C) XRD patterns of NPHPC@Sn and NPHPC-G@Sn, compared with the standard diffraction peaks for *β*-Sn (JCPDS No. 04–0673). The narrow and sharp spectral width evinces that the Sn nanoparticles have good crystallinity. SEM images of NPHPC@Sn (D) and NPHPC-G@Sn (G). Insets: higher-magnification SEM image of the hybrids. TEM images of NPHPC@Sn (E) and NPHPC-G@Sn (H). Insets: higher-magnification TEM image of the corresponding samples. HRTEM images of NPHPC@Sn (F) and NPHPC-G@Sn (I). Insets: HRTEM image of a typical Sn nanoparticle in the composites.

In pursuit of achieving high performance Sn-based anodes, to date, numerous elaborate synthetic strategies have been developed so as to efficiently address the aforementioned issues. Generally, the primarily effective approaches include: (1) nanostructuring Sn-based materials with diverse fine structures to alleviate mechanical strain [12–14], (2) building intermetallic alloys or amorphous SnO_x to ease volume expansion of Sn [15–18], and (3) introducing carbon-based matrices to mitigate the volume fluctuations and inhibit mechanical fracture of Sn [19–22]. Among them, the construction of compatible carbon-based matrix/Sn hybrids is the most promising approach to solve the issues of Sn-based electrodes in view of that the carbon-based matrices can additionally contribute to the efficient electronic conduction of the entire electrode. To this end, various well-designed nanocomposites ranging from one dimensional to three dimensional architectures have been developed through delicate nanotechnology, which exhibit significantly longer cyclic lifespan compared with the pristine Sn-based particles [21,23–26]. However, their long-term cycling stability and rate capability are still far from satisfactory owing to the easy formation

of bulk Sn clusters during repeated charge/discharge, which ultimately devastates the pre-constructed nanostructures. In addition, their scalability for mass-production remains a big challenge due to the harsh reaction conditions (i.e., the requirement of explosive hydrogen gas during Sn reduction), complex synthetic procedures, high cost and/or low throughput. On the other hand, for most of the reported Sn-based anodes, especially those composites-based, there is still lack of in-depth mechanistic study on mechanism investigation. Thus, it is imperative to explore new strategies for developing advanced Sn-based anodes together with *in situ* characterization techniques to study their fundamental mechanisms, while being suitable for large-scale production towards practical applications.

In this work, we report the fabrication of a series of composites based on supersmall (sub-10 nm) Sn-based nanoparticles (i.e., Sn and SnO_2) embedded in different carbon matrices (i.e., nitrogen/phosphorus codoped hierarchically porous carbon (NPHPC) and NPHPC-reduced graphene oxide hybrid (NPHPC-G)), using facile and scalable approaches. Typically, the NPHPC@Sn and NPHPC-G@Sn composites were fabricated by a one-step *in situ* carbonization of Sn^{2+} absorbed melamine polyphosphate (MPP), whereas the NPHPC@SnO_2 and NPHPC-G@SnO_2 were obtained by a one-pot hydrothermal process, either without or with graphene oxide (GO) in the original reaction liquid. In sharp contrast to previously reported strategies that require exquisite nano-techniques and/or delicate instruments for constructing carbon/Sn nanocomposites, our work reported here only involves maturely industrial processes. At the same time, MPP, the precursor of NPHPC, is a commercially available product, which has been widely used as a non-halogen flame retardant and can be readily purchased in tons with low price or be quickly and easily synthesized in hundreds of grams with lab-scale as demonstrated in our case (Fig. S1). Therefore, mass production of these composites can be expected, which makes a significant step forward to the practical applications of Sn-based materials. More intriguingly, the distinct structure of the composites

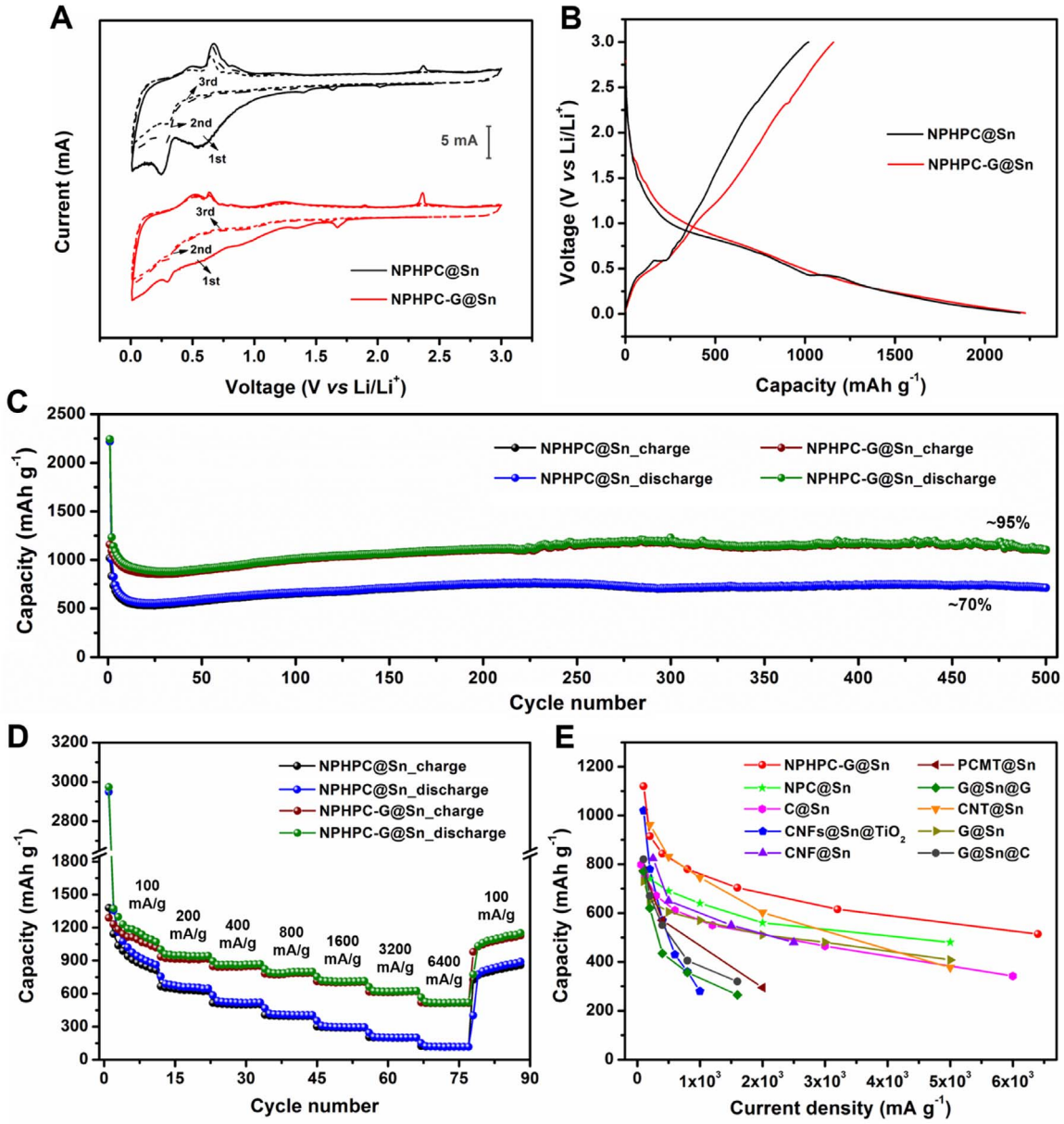

Fig. 2. Electrochemical properties of the NPHPC@Sn and NPHPC-G@Sn composites. (A) CV profiles of the NPHPC@Sn and NPHPC-G@Sn electrodes at a scan rate of 0.5 mV s^{-1} in the potential window of 0.01–3.0 V (vs Li/Li^+). The initial charge/discharge voltage profiles (B) and cycling performance (C) of NPHPC@Sn and NPHPC-G@Sn electrodes measured at 200 mA g^{-1}. (D) Rate capabilities of NPHPC@Sn and NPHPC-G@Sn electrodes under programmed current densities. (E) Specific capacity as a function of current density for NPHPC-G@Sn electrode in comparison with the reported carbon/Sn anodes.

endows excellent anodic performances for LIBs, in particular, NPHPC-G@Sn and NPHPC-G@SnO_2 exhibit good cyclic stability (maintaining a reversible capacity as high as ~1099 mAh g^{-1} after 500 cycles and ~1117 mAh g^{-1} after 300 cycles, respectively) as well as extraordinary rate capability. To the best of our knowledge, their overall performances are in the top level of Sn-based composites so far have been reported. Both *in situ* and *ex situ* techniques are successfully applied to monitor electrochemical-reaction-induced microstructural changes and understand the lithiation/delithiation mechanisms of the composites. This work provides a low-cost and effective route to construct advanced Sn-based materials, which may also shed light on the development of other carbon/metal-based hybrids for practical application, not limited to LIBs, but can also be used in a broad spectrum of electrochemical fields.

2. Results and discussion

2.1. NPHPC@Sn and NPHPC-G@Sn nanostructures

Fig. 1A schematically presents the synthesis procedure of NPHPC@Sn nanostructure by means of a one-step *in situ* carbonization of Sn^{2+} absorbed MPP, where the MPP precursor was prepared by the method reported in our recent work [27]. Briefly, $SnCl_2$ was firstly dissolved into MPP dispersion under constant stirring, during which the positively charged Sn^{2+} will be captured by the electron donating NH_2 group on MPP. The precipitation was collected, dried, and then carbonized with the protection of an argon flow (see Experimental section for details). During the annealing process, MPP was pyrolyzed into NPHPC (Fig. S2 and S3), whereas the decomposition of MPP caused an organic molecules enriched reducing atmosphere, as demonstrated by pyrolysis gas chromatography mass spectrometry (Py-GC/MS) (Fig. 1B), which simultaneously triggers Sn^{2+} *in situ* reduced to Sn nanoparticles, leading to the formation of NPHPC@Sn composite. To better confine Sn nanoparticles in the carbon matrix, and increase the conductivity of the composite, we further fabricated NPHPC-G@Sn composite, as shown in Fig. 1A (right part of the schematic image. Note: GO will be reduced solely under thermal annealing condition [28], and the amount of GO used in this work was referred to our previous work unless otherwise stated [29]). X-ray diffraction (XRD) patterns (Fig. 1C) of the as-formed composites reveal a pure phase Sn nanostructure well indexed to β-Sn (JCPDS No. 04–0673). The sharp diffraction peaks with small full width at half-maximum (FWHM) values signify good crystallinity of the Sn nanoparticles. Because of its simplicity, scalability, and most importantly the circumvention of using the explosive hydrogen gas, our present approach is significantly superior to the previous works on fabricating carbon/Sn composites [19,20,22,23], and hence more suitable for real applications. The mean size of Sn crystallites in the composites is calculated to be ~7 nm based on Scherrer equation ($t = 0.9\lambda/\beta\cos\theta$, where θ is the Bragg angle, β is FWHM in radian, λ is the X-ray wavelength, and t is the mean crystalline domain size), using Sn (100) peak. Scanning electron microscopy (SEM) images (Fig. 1D) show that the NPHPC@Sn hybrid has a coral-shaped 3D morphology and no bulk Sn aggregations are observed. Further transmission electron microscopy (TEM) images (Fig. 1E) disclose a large number of uniform-sized Sn nanoparticles that well dispersed in the 3D macroporous structure. The average size of Sn nanoparticles is around 7 nm, as evidenced by high-resolution TEM (HRTEM) images (Fig. 1F), consistent with the XRD results. Such morphological uniqueness and structural uniformity may accommodate the large strain of Sn nanoparticles; prevent their pulverization and agglomeration during lithiation/delithiation, thus affording long cyclic life. In another case, the NPHPC-G@Sn composite displays similar geometric feature in regard to NPHPC@Sn. As shown in Fig. 1G, NPHPC-G@Sn exhibits an interconnected framework with graphene perfectly integrated into the 3D matrix, which not only facilitates electrolyte-electrode interactions and charge transfer process, but also benefits to preserve the electrode integrity during cycling. TEM and HRTEM images (Fig. 1H and I) illustrate that the morphology, distribution and size of Sn nanoparticles in NPHPC-G@Sn present no apparent differences with respect to NPHPC@Sn. The weight content of carbon in NPHPC@Sn and NPHPC-G@Sn composites is determined to be 42.8 and 46.6%, respectively, according to thermogravimetric analysis (TGA, Fig. S4).

To probe the electrochemical properties of the composites, cyclic voltammetry (CV) tests were performed on coin-type cells using lithium foil as both counter and reference electrodes. As shown in Fig. 2A, the CV profiles of NPHPC@Sn electrode reproduce similar electrochemical characteristics compared with that of NPHPC-G@Sn. In the first scan, a few irreversible peaks are monitored. Specifically, the broad peak at 0.4–1.0 V corresponds to both the lithiation of Sn and SEI formation associated with electrolyte decomposition [24,30]. While the small redox peaks at ~2.4, ~1.7 and ~1.4 V are presumably due to the Li insertion and extraction from the oxygen-containing functional groups on carbon [27]. Nevertheless, from the second sweep onward, the electrochemical reactions gradually become reversible. The two cathodic peaks at ~0.25 and ~0.62 V originate from the alloying reaction of Sn to Li_xSn phase, whereas the two anodic peak at ~0.47 and ~0.67 V are assigned to the dealloying of Li_xSn to Sn [19,22]. Clearly, NPHPC-G@Sn electrode exhibits better reversibility than NPHPC@Sn, as reflected by the well overlapped CV curves, indicative of the presence of graphene is more favorable for restraining the volume variations and aggregation of Sn nanoparticles. Furthermore, the distinguishable negatively shifted anodic peaks accompanied by the positively shifted cathodic peaks of NPHPC-G@Sn electrode manifest its enhanced kinetic behaviors, namely, easier migration of Li ion through the SEI film and faster charge transfer. The electrochemical stability of the composite electrodes was evaluated by galvanostatic cycling at a current density of 200 mA g^{-1}. Fig. 2B shows the initial charge-discharge profiles of these electrodes, which express typical features of carbon/Sn anodes. The first discharge capacity of NPHPC@Sn and NPHPC-G@Sn electrode is 2194 and 2224 mAh g^{-1}, respectively, with a reversible capacity of 1019 and 1158 mAh g^{-1} retained in the subsequent charge process. The comparatively larger coulombic efficiency of NPHPC-G@Sn electrode (52.1%) compared with that of NPHPC@Sn (46.4%) states its stronger ability for confining Sn nanoparticles and accordingly eluding the detrimental reactions of Sn with Li ions, agreeing well with the CV results. Importantly, NPHPC-G@Sn electrode also possesses a high reversible capacity of 1099 mAh g^{-1} (~95% retention, and ~100% of the second cycle capacity) with a coulombic efficiency of 99.4% (Fig. S5) after 500 consecutive cycles (Fig. 2C), which is far superior than that of NPHPC@Sn (711 mAh g^{-1}, ~70% retention). Galvanostatic charge-discharge measurements were further conducted at varied current densities to assess their rate capability (Fig. 2D and Fig. S6). The average reversible capacity of NPHPC-G@Sn electrode reaches as high as 1120, 915, 844, 780, 704, 615 and 514 mAh g^{-1} at programmed current rates of 100, 200, 400, 800, 1600, 3200 and 6400 mA g^{-1}, respectively. All of these values are considerably higher than those of NPHPC@Sn (i.e., 877, 579, 458, 361, 266, 182 and 108 mAh g^{-1} sequentially tested at 100, 200, 400, 800, 1600, 3200 and 6400 mA g^{-1}), especially at higher current rate, for example, > 800 mA g^{-1}, once again documenting the faster kinetics of electrochemical reactions in NPHPC-G@Sn electrode. This matches well with the electrochemical impedance spectroscopy (EIS) results shown in Fig. S7. It is worth emphasizing that even after a deep cycling at an extremely high current rate of 6400 mA g^{-1}, the reversible capacity of NPHPC-G@Sn can be instantly recovered to 978 mAh g^{-1} when the current abruptly switches back to 100 mA g^{-1}, and progressively approaches to its former values upon cycling, which exclusively proofs its superb rate capability. These amazing electrochemical performances are definitely beyond the previously reported carbon/Sn anodes (Fig. 2E), for example, Sn-embedded nitrogen-doped porous carbon (NPC@Sn) [30], hierarchical Sn/Carbon hybrid (C@Sn) [19], Sn nanopillar arrays embedded graphene (G@Sn) [24], Sn-encapsulated porous carbon

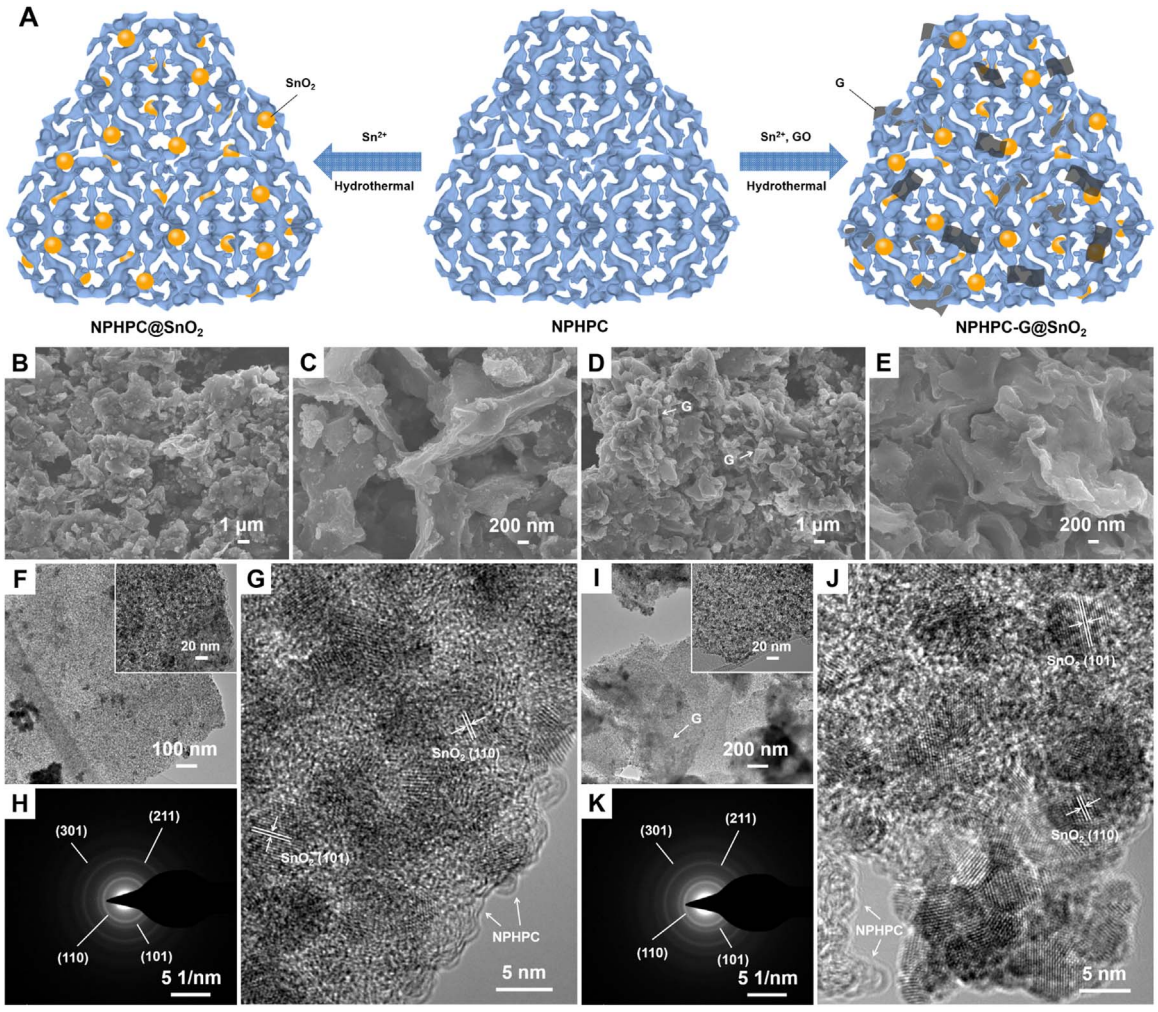

Fig. 3. Schematic diagrams of fabrication and morphological characterizations of the NPHPC@SnO_2 and NPHPC-G@SnO_2. (A) Schematic of the synthetic process of NPHPC@SnO_2 and NPHPC-G@SnO_2 by hydrothermal reaction. SEM images of NPHPC@SnO_2 (B and C) and NPHPC-G@SnO_2 (D and E) nanostructures with different magnifications. (F) TEM image of NPHPC@SnO_2. Inset: the corresponding TEM image with higher-magnification. (G) HRTEM image of NPHPC@SnO_2. (H) SAED pattern of NPHPC@SnO_2. (I) TEM image of NPHPC-G@SnO_2. Inset: the corresponding TEM image with higher-magnification. (J) HRTEM image of NPHPC-G@SnO_2. (K) SAED pattern of NPHPC-G@SnO_2. The lattice spacing of 0.33 and 0.26 nm in the HRTEM images (G and J) corresponds to the (110) and (101) planes of rutile SnO_2, respectively. Indexing of the rings in SAED patterns (H and K), from inner to outer ring, could be successively indexed to the (110), (101), (211), and (301) planes of rutile SnO_2.

microtubes (PCMT@Sn) [23], Sn sandwiched graphene (G@Sn@G) [21], TiO_2-coated Sn/carbon nanofibers (CNFs@Sn@TiO_2) [31], Sn-encapsulated carbon nanotubes (CNT@Sn) [20], Sn-embedded carbon nanofibers (CNF@Sn) [32], and Sn/carbon nanocables integrated graphene (G@Sn@C) [25].

2.2. *NPHPC@SnO_2 and NPHPC-G@SnO_2 nanostructures*

The NPHPC@SnO_2 and NPHPC-G@SnO_2 nanohybrids were synthesized via a hydrothermal method, using NPHPC (the pyrolysis product of MPP) and $SnCl_2$ as the precursors, either without or with GO in the original reaction liquid (Fig. 3A). This process involves the hydrolysis and oxidation of $SnCl_2$ to produce SnO_2 [33,34] and, at the same time, GO undergoes a superheated-H_2O-promoted deoxidation reaction to transform into graphene [35]. SEM images of NPHPC@SnO_2 (Fig. 3B and C) reveal that the obtained SnO_2 nanoparticles are firmly anchored on the carbon nanowalls with a few aggregations non-uniformly dispersed among the voids of the NPHPC matrix. Interestingly, NPHPC-G@SnO_2 exhibits a wrinkled structure composing of highly curved graphene filled in the interspaces of NPHPC, with non-aggregated nanocrystals exposed on the outer surfaces (Fig. 3D and E). TEM and HRTEM images further manifest that the SnO_2 nanoparticles bound to NPHPC and NPHPC-G have a typical size of 3–7 nm (Fig. 3G and F) and 4–5 nm (Fig. 3I and J), respectively. The corresponding selected-area electron diffraction (SAED) patterns (Fig. 3H and K) with a ring-like mode can be indexed to the tetragonal rutile-type structure of SnO_2 (JCPDS No. 41–1445), in accordance with the XRD results (Fig. S8). Raman spectrum of NPHPC@SnO_2 hybrid (Fig. S9) shows almost the same I_D/I_G value (1.01) compared with that of NPHPC (1.00), and no relative shifts of D and G bands are observed, indicative of no structural change after SnO_2 nanoparticles deposition. However, in the case of NPHPC-G@SnO_2, markedly sharper D and G Raman features with larger I_D/I_G value (1.03) are noted, attributable to the additionally introduced graphene with high reduction degree [36]. To quantify the composition of the hybrids, TGA was conducted in air over a temperature ranging from room temperature to 800 °C (Fig. S10). The weight content of carbon is calculated to be 25.5% for NPHPC@SnO_2 and 31.1% for NPHPC-G@SnO_2. N_2 sorption measurements (Fig. S11) illustrate type-IV isotherms with a small hysteresis loop for both of the hybrids, belonging to the distinctive characteristics of mesoporous materials [37]. The details of corresponding pore structure parameters, including Brunauer-Emmett-Teller surface area, total pore volume, and average pore diameter, are summarized in Table S1. It is noteworthy that porous structure is beneficial for loading active nanoparticles and tolerating the associated volume changes during cycling, facilitating electrolyte penetration, as well as favoring Li ions

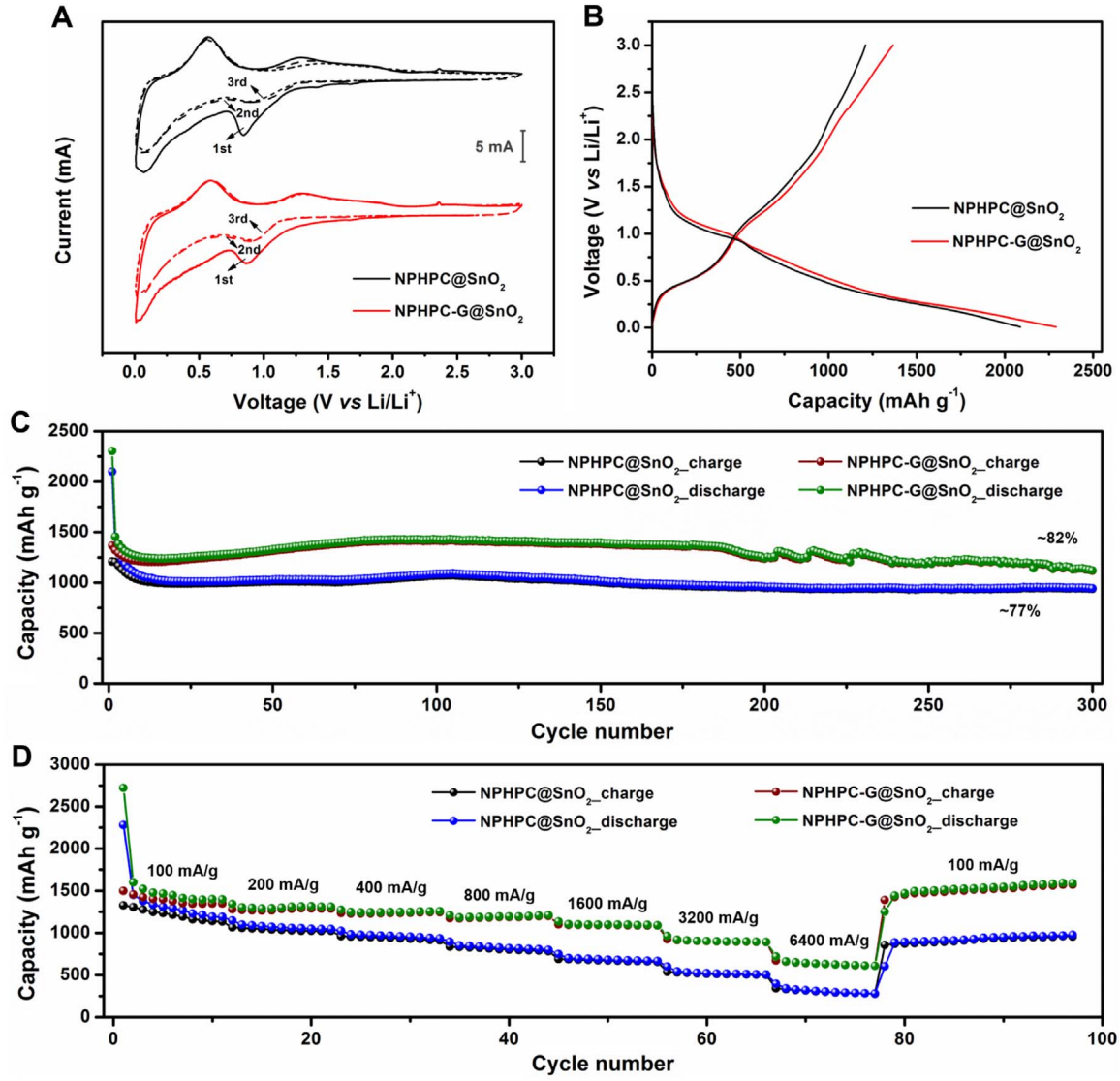

Fig. 4. Electrochemical properties of the NPHPC@SnO_2 and NPHPC-G@SnO_2 composites. (A) CV profiles of the NPHPC@SnO_2 and NPHPC-G@SnO_2 electrodes at a scan rate of 0.5 mV s^{-1} in the potential window of 0.01–3.0 V (vs Li/Li^+). The initial charge/discharge voltage profiles (B) and cycling performance (C) of NPHPC@SnO_2 and NPHPC-G@SnO_2 electrodes measured at 200 mA g^{-1}. (D) Rate capabilities of NPHPC@SnO_2 and NPHPC-G@SnO_2 electrodes under programmed current densities.

diffusion, and therefore the hybrids are expected to show long-term cycling behavior for LIBs.

Fig. 4A depicts the CV characteristics for the NPHPC@SnO_2 and NPHPC-G@SnO_2 electrodes. The predominant cathodic peak at ~0.87 V in the initial scan corresponds to SEI formation on the electrode and the conversion of SnO_2 to Sn [26,38]. This peak is substituted by a newly emerged one at ~0.92 V in the following scans, which can be exclusively ascribed to the conversion reaction of SnO_2 [39]. Another cathodic peak at ~0.08 V is assigned to the alloying reaction of Sn [40], yielding various Li_xSn alloys. Accordingly, the anodic peaks at ~0.57 and ~1.29 V are sequentially attributed to Li_xSn dealloying reaction and the conversion reaction of Sn to generate SnO_2 [38,39]. In contrast to the partially overlapped CV curves of NPHPC@SnO_2, after the first cycle, the CV curves of NPHPC-G@SnO_2 are perfectly overlapped, documenting its better reversibility for electrochemical reactions. Moreover, the correlative plateau regions of the electrodes could be identified from the charge-discharge profiles as well (Fig. 4B). The initial coulombic efficiency of NPHPC-G@SnO_2 electrode is 59.7% (with a charge and discharge capacity of 1366 and 2289 mAh g^{-1}, respectively, at 200 mA g^{-1}), a bit larger than that of NPHPC@SnO_2 (57.9%), evidencing the existence of graphene is beneficial for suppressing the detrimental side reactions, for example, the irreversible conversion reactions between SnO_2 and Sn, and electrolyte decomposition reactions. Electrochemical stability of the electrodes was examined under galvanostatic cycling at a current density of 200 mA g^{-1} (Fig. 4C). For NPHPC@SnO_2 electrode, the initial reversible capacity is 1209 mAh g^{-1}, which stabilized at 937 mAh g^{-1} after 300 cycles with a coulombic efficiency of 99.4% (Fig. S12). Instead, NPHPC-G@SnO_2 exhibits much higher capacity throughout the entire cycles, with a reversible capacity of up to 1117 mAh g^{-1} is retained after 300 cycles (99.6% coulombic efficiency), indicative of the combined effects of NPHPC-G nanostructure in promoting the conversion reactions between SnO_2 and Sn. In addition, the rate performance of these hybrids was evaluated under a series of current rates (Fig. 4D and Fig. S13). As the current rate increased successively from 100, 200, 400, 800, 1600 and 3200 mA g^{-1}, the average reversible capacity of NPHPC-G@SnO_2 is determined to be 1390, 1279, 1236, 1185, 1092 and 902 mAh g^{-1}, respectively. Even under a high current rate of 6400 mA g^{-1}, the electrode still shows steady-state capacity, capable of delivering an average reversible capacity as high as 634 mAh g^{-1}, 45.6% of that at 100 mA g^{-1}. These values are undeniably larger than those of NPHPC@SnO_2, which is the results of lower Li ion migration resistance and charge transfer resistance in NPHPC-G@SnO_2 electrode, as demonstrated by EIS analysis (Fig. S14). Strikingly, upon switching the

current density back to 100 mA g^{-1}, the capacity was able to immediately revert to 1390 mAh g^{-1}, fully recovering to the original value. Such exceptional electrochemical behaviors are superior to the recently reported SnO_2-based anodes that summarized in Table S2.

The above distinguished electrochemical properties in NPHPC-G@Sn and NPHPC-G@SnO_2 hybrids are attributed to their unique nanoscale complex architectures. First, the small-sized Sn-based nanoparticles (< 10 nm) provide numerous active sites for Li storage without causing any severe deterioration of the electrode because of the nanometer size effects, that is, small mechanical stresses/strains during electrochemical reactions and considerably decreased solid-state diffusion length for Li ions. Meanwhile, these nanosized particles anchored tightly on the carbon matrix are helpful for restricting the movement of Sn, and therefore restrains the generation of bulk Sn clusters during alloying/dealloying processes, if any, they are still trapped within the interconnected porous network of the carbon matrix, maintaining good electrical contact. Second, the robust and conductive carbon framework not only ensures fast and efficient electron transport, but also is beneficial to retain the structural integrity of the composite electrode throughout cycling. Moreover, the porous nature of the composites allows for high accessibility to electrolyte and fast Li ions transport, and more importantly, capable of effectively accommodating the volume variations of the Sn-based nanoparticles. Third, the amazing structure of NPHPC contributes significantly to the eventual high capacity of the hybrids (Fig. S15), while the integrated graphene sheets are favorable for better confining the Sn-based nanoparticles and simultaneously afford fast electrochemical reaction kinetics of Li ions and electrons.

2.3. *In situ* TEM and ex situ SEM studies

To directly visualize electrochemical-reaction-induced microstructural changes and understand the lithiation/delithiation mechanisms of the composites, we have successfully constructed a series of nanobatteries inside the TEM (details are given in the Experimental section) [41]. Fig. 5A-C and Movie S1 show the real-time observation of the first lithiation/delithiation processes in NPHPC-G@Sn composite upon applying a bias of 3.0 V. As shown in Movie S1, the size of the Sn nanoparticles increases with the lithiation proceeded, leading to a volume expansion of about 190% in the lithiated bulk structures (Fig. 5B). Correspondingly, the SAED changes from characteristic spots of single crystalline β-Sn phase to ring patterns of $Li_{13}Sn_5$ nanocrystallines dispersed in the Li_2O matrix (Insets of Fig. 5A and B). The Li_2O nanoparticles are originated from Li reaction with the oxygen-containing groups in NPHPC-G, as detected by the previous CV curves (Fig. 2A). Immediately after reversing the bias, Li starts to

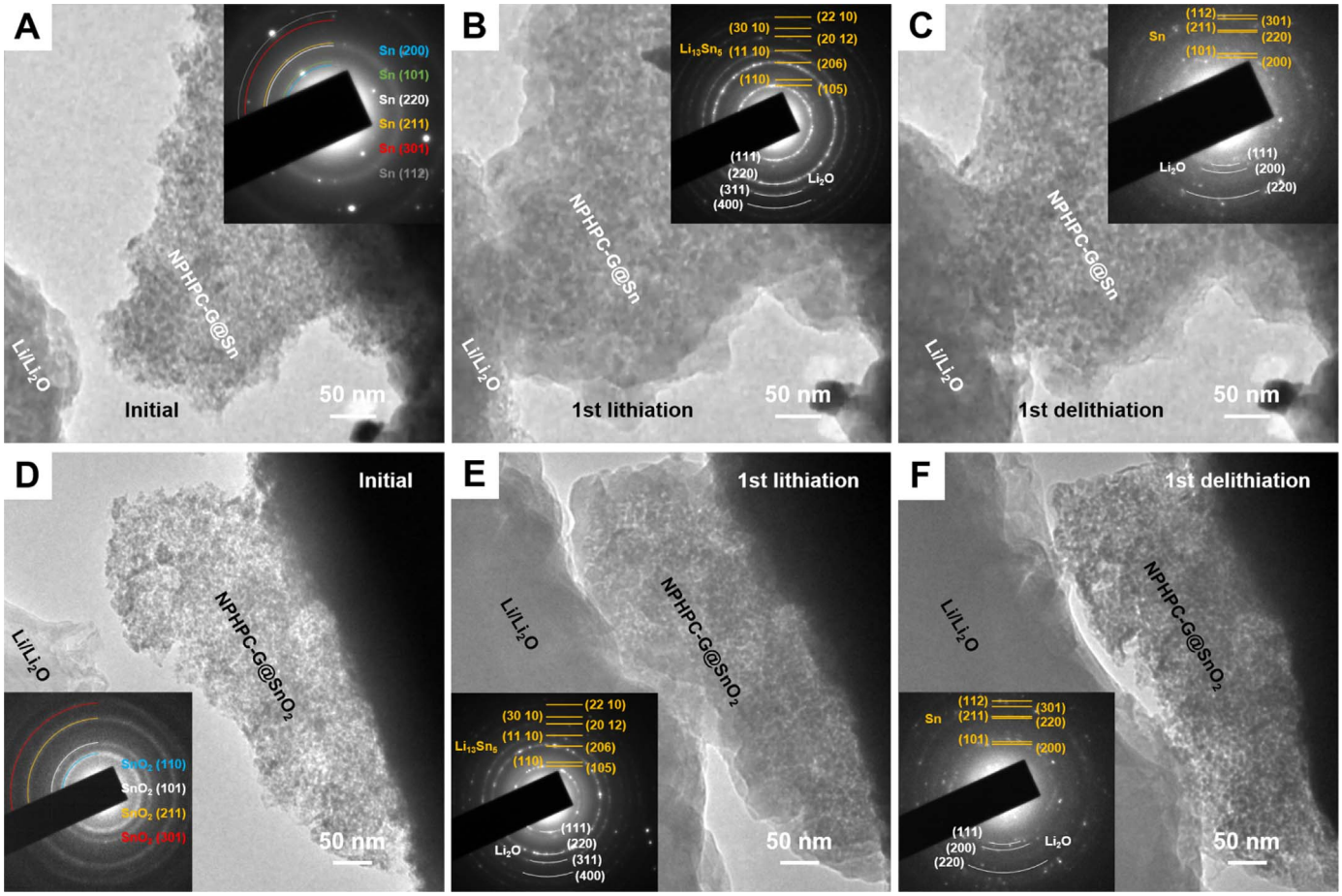

Fig. 5. *In situ* TEM studies of structural evolution of NPHPC-G@Sn and NPHPC-G@SnO_2 during lithiation/delithiation processes. (A) TEM image of NPHPC-G@Sn before electrochemical cycling (initial). The corresponding SAED pattern displays spotty rings characteristic, representative of β-Sn phase. (B) TEM image of the lithiated NPHPC-G@Sn, showing ~190% volume expansion. The SAED shows superimposed diffraction rings, corresponding to $Li_{13}Sn_5$ nanocrystallines (orange indices) within the Li_2O matrix (white indices). (C) TEM image of the delithiated NPHPC-G@Sn featuring the maintenance of the overall morphology of NPHPC-G@Sn as its initial stage. The SAED rings can be indexed as β-Sn (orange indices) and irreversible Li_2O (white indices), indicative of the $Li_{13}Sn_5$ alloy was converted back to Sn. TEM images of NPHPC-G@SnO_2 before cycling (D), after lithiation (E), and after delithiation (F), revealing good structural integrity of NPHPC-G@SnO_2 during electrochemical reactions. The SAED of pristine NPHPC-G@SnO_2 is indexed as rutile SnO_2 (inset of D). Following the conversion and then alloying processes, $Li_{13}Sn_5$ (orange indices) and Li_2O nanocrystallines (white indices) are presented after lithiation (inset of E). In the subsequent delithiation, the SAED (inset of F) shows ring patterns stemming from dealloying reaction produced β-Sn (orange indices) and the irreversible Li_2O (white indices), matching well with previous works [10,43,44].

extract from the composite, and accordingly the monoliths contract until the nanoparticles are distinctly detected. The SAED of the fully delithiated sample (Inset of Fig. 5C) reveals the conversion of $Li_{13}Sn_5$ alloy back to pure Sn accompanied by some incompletely extracted Li_2O nanocrystallines in the hybrid. In the subsequent repetitive cycles, the Sn nanoparticles can still reversibly react with Li indicated by the size variations during lithiation and delithiation processes. Notably, the overall structure of the composite is preserved as shown in Fig. S16A and S16B. These results not only suggest the structural uniqueness of our NPHPC-G@Sn composite but also prove the robust mechanical stability of the NPHPC-G matrix in accommodating the volume changes of Sn nanoparticles during electrochemical reactions. Similar phenomenon was also observed in the case of NPHPC-G@SnO_2, where Li ions reversibly inserted in and extracted from the composite while the composite maintains its overall morphology (Fig. 5D-F, Fig. S16C and S16D). The details of *in situ* TEM study illustrating electrochemical behaviors of NPHPC-G@Sn and NPHPC-G@SnO_2 are shown in Movie S1 and S2, respectively. Based on the results, we note that although the Sn-based nanoparticles exhibit large volume changes, they remain firmly anchored on the NPHPC-G matrix and do not show visible aggregations. This ensures good electrical connection and mechanical stability during cycling. The excellent electrode integration is believed to be responsible for the long-term cyclic performance with minimal capacity decay of the NPHPC-G@Sn and NPHPC-G@SnO_2 electrodes.

Supplementary material related to this article can be found online at http://dx.doi.org/10.1016/j.ensm.2018.02.008.

In addition to *in situ* TEM, we also performed *ex situ* SEM investigations on the cycled hybrid anodes to understand the structural features of the composites. As shown in Fig. S17, a uniform and compact SEI layer was discovered on the surface of both electrodes after 100 cycles, which can prohibit further electrolyte decomposition, and is also critical for achieving long-term cyclability. Meanwhile, the cycled electrodes display good structural integrity without cleavages, and no detectable structural collapse or damage of the hybrids is observed (Insets of Fig. S17), indicative of effectively accommodating the volume changes of Sn-based nanoparticles within the carbon matrices. Scanning transmission electron microscopy (STEM) images and the corresponding energy-dispersive X-ray spectroscopy (EDS) mapping (Fig. S18) further disclose that the integrated frameworks with homogeneously distributed Sn-based nanoparticles are well maintained after cycling, demonstrating the successful suppression of nanoparticles aggregation during electrochemical processes, consistent with the *in situ* TEM results (Fig. 5). Accordingly, even if any bulk Sn clusters are generated upon prolonged cycles, they will be still confined in the porous carbon networks whilst preserving good electrical contact with the electrode components, thus enabling long-cyclic performance.

Prototype full-cell devices comprising a commercial lithium iron phosphate (LFP) cathode (detailed information is given in Fig. S19) and the Sn-based hybrid anodes were built to appraise the potential viability of the composites. The voltage profiles of the fabricated NPHPC-G@Sn/LFP and NPHPC-G@SnO_2/LFP full-cells both show combined characteristics of the flat-shaped LFP cathode and the sloppy-shaped hybrid anodes with an average voltage of ~2.2 V, and in the meantime the reversible capacity is determined to be 72 mAh g^{-1} for NPHPC-G@Sn/LFP and 78 mAh g^{-1} for NPHPC-G@SnO_2/LFP at a current rate of 1 C (170 mA g^{-1} vs LFP, Fig. S20). Excitingly, two tandem cells based on NPHPC-G@Sn/LFP and NPHPC-G@SnO_2/LFP in series, after being cycled 10 times at a C/20 rate, have been successfully used to power 20 parallel-connected red light-emitting diodes (LED) for more than 1 h (Fig. S21), highlighting the great potential of our NPHPC-G@Sn and NPHPC-G@SnO_2 composites for advanced battery applications. We note that although the cycling stability of the cells is now not satisfactory due to the low initial coulombic efficiency the composites, this can be potentially improved by refining the skill for full-cell fabrication and employing prelithiation technique, which have been marked as important aspects for our future studies.

3. Conclusions

In summary, we have successfully demonstrated high-performance anodes composed of sub-10 nm Sn-based nanoparticles (i.e., Sn and SnO_2) embedded in functionalized carbon frameworks (i.e., NPHPC and NPHPC-G) for LIBs. Particularly, the NPHPC-G@Sn and NPHPC-G@SnO_2 hybrids with additionally introduced graphene possess fast kinetics of electrochemical reactions, consequently affording long-cyclic performance (> 300 cycles without significant capacity decay) and superior rate capability. *In situ* TEM and *ex situ* SEM studies were carried out to elucidate structural features of the composites upon electrochemical reactions, both of which disclose that the integrated carbon network can effectively buffer the mechanical stress stems from the volume variations of Sn-based nanoparticles, and hence leading to stable electrochemical cycling. Our protocols for the synthesis of carbon/Sn hybrids are scalable and compatible with the industrial manufacturing technology, which will potentially allow for large-scale production towards practical applications, not only in LIBs but also the emerging sodium-ion batteries and other energy fields. Importantly, the techniques would be generally applicable to other alloy-type materials, such as Sb and Ge, which also encounters huge-volume-changes-induced capacity fading.

4. Experimental section

4.1. Fabrication of NPHPC@Sn and NPHPC-G@Sn

The NPHPC@Sn was prepared by *in situ* carbonization of Sn^{2+} absorbed MPP. In a typical synthesis, 7 g MPP was dispersed in 400 mL deioned water by sonication for 30 min under constant mechanical stirring. Subsequently, 100 mg of $SnCl_2{\cdot}2H_2O$ was dissolved into the suspension with vigorous magnetic stirring for 3 h. The resulting mixture was filtered through a cellulose acetate membrane filter (pore: 0.22 μm, diameter: 50 mm) and dried overnight in an electric oven at 80 °C. Finally, the precursor was pyrolyzed at 900 °C for 2 h in argon atmosphere with a heating rate of 5 °C min^{-1} and a gas flow rate of 100 sccm. The NPHPC-G@Sn was prepared in the same way except that 7 mL of 5 mg mL^{-1} GO aqueous solution was dropwise added into the mixture after $SnCl_2{\cdot}2H_2O$ was dissolved into the MPP suspension for 2 h.

4.2. Fabrication of NPHPC@SnO_2 and NPHPC-G@SnO_2

The NPHPC was prepared following the same procedure reported in our previous work [27,42]. Then NPHPC aqueous dispersion, composing of 25 mg NPHPC and 3 mg sodium dodecyl sulfate in 70 mL deioned water, was prepared by sonication for 10 min. Subsequently, 113 mg of $SnCl_2{\cdot}2H_2O$ was added into the dispersion with continuous magnetic stirring for 5 min. The resulting mixture was sealed in a 80 mL Teflon autoclave for hydrothermal reaction at 180 °C for 12 h. Finally, the NPHPC@SnO_2 precipitate was collected by filtration and repeatedly washed with deioned water prior to be dried in an electric oven at 80 °C. The NPHPC-G@SnO_2 was prepared following the same procedure except an extra adding of 10 mg GO in the aforementioned NPHPC aqueous dispersion.

4.3. Characterization

Powder XRD patterns were taken using a Bruker D8 Advance diffractometer with Cu Kα radiation (λ = 1.54056 Å). Py-GC/MS was carried out on NETZSCH thermal analysis instrument (STA 449 F3 Jupiter®) coupled with QMS 403 D Aëolos® gas analysis system. Flash pyrolysis was conducted at 700 °C for 30 s. GC oven conditions were programmed at 50 °C for 5 min, increased to 270 °C with a ramping rate of 15 °C min^{-1}, and isothermal for 8 min. The carrier gas (helium, purity 99.999%) was in a constant flow mode of 20 mL min^{-1}. MS was

performed from m/z 30 to m/z 400 with a scan time of 0.2 s, and the MS transfer line temperature was 270 °C. X-ray photoelectron spectroscopy (XPS) was characterized using an ESCALAB MK II instrument with Al Kα radiation. SEM images were performed on a JEOL JSM-6700F scanning electron microscope. TEM images were recorded on a FEI Tecnai F20 transmission electron microscope operated at 200 kV. N_2 adsorption and desorption analysis was acquired on a Micromeritics ASAP 2020 instrument at 77 K. Raman spectra were conducted on a WITec Alpha300 Series confocal Raman system with Nd:YAG laser. TGA was measured on a DTG 60 H analyzer in air atmosphere. STEM and elemental mapping images were performed on a Zeiss Auriga Dual-Beam FIB/SEM coupled with EDS.

In situ lithiation/delithiation observations were carried out inside an aberration-corrected STEM (JEOL JEM-ARM200CF) using sample loaded Au rod as the cathode, Li_2O coated Li metal as the solid electrolyte, and Li metal as the anode. After touching the anode with the cathode, lithiation and delithiation of the working electrode could be triggered by applying −3 and 3 V biases, respectively. The steps of electrochemical reactions can be controlled by retracting the Li anode and electrolyte. For *ex situ* SEM measurements, all the coin cells with fully charged state were disassembled inside a MBRAUN glovebox (H_2O and $O_2 < 0.1$ ppm) filled with pure argon gas (purity 99.999%). The obtained working electrodes were washed thoroughly by dimethyl carbonate (anhydrous, Sigma-Aldrich), dried in the glovebox and then transferred out for SEM characterization.

4.4. Electrochemical measurements

Electrochemical measurements were conducted on CHI 760D electrochemical workstation and NEWARE battery analyzer. CR2032 coin cells were used to investigate the Li storage properties of the materials using lithium foil as the counter electrode, Celgard® 2400 polypropylene member as the separator and 1 M $LiPF_6$ in a mixed solvent ($V_{(ethylene\ carbonate)}$:$V_{(ethyl\ methyl\ carbonate)}$:$V_{(dimethyl\ carbonate)}$ = 1:1:1) as the electrolyte. The preparation of working electrodes first involves the dispersion of active material, acetylene black and polyvinylidene fluoride (PVDF) in a weight ratio of 8:1:1 into N-methyl-2-pyrrolidinone solvent to form a slurry, and subsequently spread on a copper foil. After vacuum drying at 100 °C, the electrodes were punched out by a punching machine and weighed on a highly accurate electronic balance (0.01 mg readability). The active material loaded on one single electrode is ~1 mg cm^{-2} (1.2 cm in diameter), and the electrochemical data (e.g., current densities and specific capacities) were calculated based on the total mass of the composites. All cells were assembled in the glovebox and then aged for 12 h prior to electrochemical studies.

The full cells were designed with a negative (anode) to positive (cathode) capacity ratio of ~1.0. The LFP cathode electrode was prepared by casting the slurry comprising 80 wt% LFP, 10 wt% acetylene black and 10 wt% PVDF on an aluminum current collector. The electrode was dried in vacuum at 100 °C overnight, and the mass loading was typically ~3–4 mg cm^{-2}. All the cells were assembled under the same conditions of the half-cell mentioned above. Electrochemical tests were performed in the voltage window between 0.9 and 3.9 V, and the specific capacities were calculated referring to the mass of LFP cathode.

Acknowledgments

We thank Dr. Taixing Tan and Professor Jianfeng Zhao for technical assistance. T.Y. acknowledges the support from the Ministry of Education of Tier 1 (RG100/15, RG178/15). W.H. thanks the support by the Natural Science Foundation of Jiangsu Province (BM2012010), Priority Academic Program Development of Jiangsu Higher Education Institutions (YX03001), Ministry of Education of China (IRT1148), Synergetic Innovation Center for Organic Electronics and Information Displays, and the National Natural Science Foundation of China (61136003, 51173081). R.S.Y. acknowledges the support from the National Science Foundation (Award No. DMR-1620901). The acquisition of the UIC JEOL JEM-ARM200CF was supported by a MRI-R2 grant from the National Science Foundation (Award No. DMR-0959470).

Appendix A. Supporting information

Supplementary data associated with this article can be found in the online version at doi:10.1016/j.ensm.2018.02.008.

References

[1] S. Chu, Y. Cui, N. Liu, The path towards sustainable energy, Nat. Mater. 16 (1) (2017) 16–22.
[2] R.F. Service, The battery builder, Science 352 (6289) (2016) 1046–1049.
[3] J.M. Tarascon, M. Armand, Issues and challenges facing rechargeable lithium batteries, Nature 414 (6861) (2001) 359–367.
[4] M. Armand, J.M. Tarascon, Building better batteries, Nature 451 (7179) (2008) 652–657.
[5] W. Ai, Z. Luo, J. Jiang, J. Zhu, Z. Du, Z. Fan, et al., Nitrogen and sulfur codoped graphene: multifunctional electrode materials for high-performance Li-ion batteries and oxygen reduction reaction, Adv. Mater. 26 (35) (2014) 6186–6192.
[6] W. Ai, W. Zhou, Z. Du, C. Sun, J. Yang, Y. Chen, et al., Toward high energy organic cathodes for Li-ion batteries: a case study of vat dye/graphene composites, Adv. Funct. Mater. 27 (19) (2017) 1603603.
[7] B. Wang, B. Luo, X. Li, L. Zhi, The dimensionality of Sn anodes in Li-ion batteries, Mater. Today 15 (12) (2012) 544–552.
[8] H. Tian, F. Xin, X. Wang, W. He, W. Han, High capacity group-IV elements (Si, Ge, Sn) based anodes for lithium-ion batteries, J. Mater. 1 (3) (2015) 153–169.
[9] Y. Idota, T. Kubota, A. Matsufuji, Y. Maekawa, T. Miyasaka, Tin-based amorphous oxide: a high-capacity lithium-ion-storage material, Science 276 (5317) (1997) 1395–1397.
[10] J.Y. Huang, L. Zhong, C.M. Wang, J.P. Sullivan, W. Xu, L.Q. Zhang, et al., In situ observation of the electrochemical lithiation of a single SnO_2 nanowire electrode, Science 330 (6010) (2010) 1515–1520.
[11] M. Ebner, F. Marone, M. Stampanoni, V. Wood, Visualization and quantification of electrochemical and mechanical degradation in Li ion batteries, Science 342 (6159) (2013) 716–720.
[12] L. Xu, C. Kim, A.K. Shukla, A. Dong, T.M. Mattox, D.J. Milliron, et al., Monodisperse Sn nanocrystals as a platform for the study of mechanical damage during electrochemical reactions with Li, Nano Lett. 13 (4) (2013) 1800–1805.
[13] K. Kravchyk, L. Protesescu, M.I. Bodnarchuk, F. Krumeich, M. Yarema, M. Walter, et al., Monodisperse and inorganically capped Sn and Sn/SnO_2 nanocrystals for high-performance Li-ion battery anodes, J. Am. Chem. Soc. 135 (11) (2013) 4199–4202.
[14] M.-S. Park, G.-X. Wang, Y.-M. Kang, D. Wexler, S.-X. Dou, H.-K. Liu, Preparation and electrochemical properties of SnO_2 nanowires for application in lithium-ion batteries, Angew. Chem. Int. Ed. 46 (5) (2007) 750–753.
[15] X.-L. Wang, M. Feygenson, H. Chen, C.-H. Lin, W. Ku, J. Bai, et al., Nanospheres of a new intermetallic $FeSn_5$ phase: synthesis, magnetic properties and anode performance in Li-ion batteries, J. Am. Chem. Soc. 133 (29) (2011) 11213–11219.
[16] M.G. Kim, S. Sim, J. Cho, Novel core-shell Sn-Cu anodes for lithium rechargeable batteries prepared by a redox-transmetalation reaction, Adv. Mater. 22 (45) (2010) 5154–5158.
[17] M.I. Bodnarchuk, K.V. Kravchyk, F. Krumeich, S. Wang, M.V. Kovalenko, Colloidal tin-germanium nanorods and their Li-ion storage properties, ACS Nano 8 (3) (2014) 2360–2368.
[18] X.-L. Wang, M. Feygenson, M.C. Aronson, W.-Q. Han, Sn/SnOx core-shell nanospheres: synthesis, anode performance in Li ion batteries, and superconductivity, J. Phys. Chem. C 114 (35) (2010) 14697–14703.
[19] X. Huang, S. Cui, J. Chang, P.B. Hallac, C.R. Fell, Y. Luo, et al., A hierarchical tin/carbon composite as an anode for lithium-ion batteries with a long cycle life, Angew. Chem. Int. Ed. 54 (5) (2015) 1490–1493.
[20] X. Zhou, L. Yu, X.-Y. Yu, X.W. Lou, Encapsulating Sn nanoparticles in amorphous carbon nanotubes for enhanced lithium storage properties, Adv. Energy Mater. 6 (22) (2016) 1601177.
[21] B. Luo, B. Wang, X. Li, Y. Jia, M. Liang, L. Zhi, Graphene-confined Sn nanosheets with enhanced lithium storage capability, Adv. Mater. 24 (26) (2012) 3538–3543.
[22] Y. Xu, Q. Liu, Y. Zhu, Y. Liu, A. Langrock, M.R. Zachariah, et al., Uniform nano-Sn/C composite anodes for lithium ion batteries, Nano Lett. 13 (2) (2013) 470–474.
[23] Y. Yu, L. Gu, C. Zhu, P.A. van Aken, J. Maier, Tin Nanoparticles encapsulated in porous multichannel carbon microtubes: preparation by single-nozzle electrospinning and application as anode material for high-performance Li-based batteries, J. Am. Chem. Soc. 131 (44) (2009) 15984–15985.
[24] L. Ji, Z. Tan, T. Kuykendall, E.J. An, Y. Fu, V. Battaglia, et al., Multilayer nanoassembly of Sn-nanopillar arrays sandwiched between graphene layers for high-capacity lithium storage, Energy Environ. Sci. 4 (9) (2011) 3611–3616.
[25] B. Luo, B. Wang, M. Liang, J. Ning, X. Li, L. Zhi, Reduced graphene oxide-mediated growth of uniform tin-core/carbon-sheath coaxial nanocables with enhanced

lithium ion storage properties, Adv. Mater. 24 (11) (2012) 1405–1409.
[26] J. Liang, X.-Y. Yu, H. Zhou, H.B. Wu, S. Ding, X.W. Lou, Bowl-like SnO_2@carbon hollow particles as an advanced anode material for lithium-ion batteries, Angew. Chem. Int. Ed. 53 (47) (2014) 12803–12807.
[27] W. Ai, X. Wang, C. Zou, Z. Du, Z. Fan, H. Zhang, et al., Molecular-level design of hierarchically porous carbons codoped with nitrogen and phosphorus capable of in situ self-activation for sustainable energy systems, Small 13 (8) (2017) 1602010.
[28] S. Pei, H.-M. Cheng, The reduction of graphene oxide, Carbon 50 (9) (2012) 3210–3228.
[29] W.W. Zhou, J.X. Zhu, C.W. Cheng, J.P. Liu, H.P. Yang, C.X. Cong, et al., A general strategy toward graphene@metal oxide core-shell nanostructures for high-performance lithium storage, Energy Environ. Sci. 4 (12) (2011) 4954–4961.
[30] Z. Zhu, S. Wang, J. Du, Q. Jin, T. Zhang, F. Cheng, et al., Ultrasmall Sn nanoparticles embedded in nitrogen-doped porous carbon as high-performance anode for lithium-ion batteries, Nano Lett. 14 (1) (2014) 153–157.
[31] M. Mao, F. Yan, C. Cui, J. Ma, M. Zhang, T. Wang, et al., Pipe-wire TiO_2-Sn@carbon nanofibers paper anodes for lithium and sodium ion batteries, Nano Lett. 17 (6) (2017) 3830–3836.
[32] Y. Yu, L. Gu, C. Wang, A. Dhanabalan, P.A. van Aken, J. Maier, Encapsulation of Sn@carbon nanoparticles in bamboo-like hollow carbon nanofibers as an anode material in lithium-based batteries, Angew. Chem. Int. Ed. 48 (35) (2009) 6485–6489.
[33] C. Wang, Y. Zhou, M. Ge, X. Xu, Z. Zhang, J.Z. Jiang, Large-scale synthesis of SnO_2 nanosheets with high lithium storage capacity, J. Am. Chem. Soc. 132 (1) (2010) 46–47.
[34] H. Wang, A.L. Rogach, Hierarchical SnO_2 nanostructures: recent advances in design, synthesis, and applications, Chem. Mater. 26 (1) (2014) 123–133.
[35] Y. Zhou, Q. Bao, L.A.L. Tang, Y. Zhong, K.P. Loh, Hydrothermal dehydration for the "green" reduction of exfoliated graphene oxide to graphene and demonstration of tunable optical limiting properties, Chem. Mater. 21 (13) (2009) 2950–2956.
[36] W. Ai, J. Jiang, J. Zhu, Z. Fan, Y. Wang, H. Zhang, et al., Supramolecular polymerization promoted in situ fabrication of nitrogen-doped porous graphene sheets as anode materials for Li-ion batteries, Adv. Energy Mater. 5 (15) (2015) 1500559.
[37] V. Meynen, P. Cool, E.F. Vansant, Verified syntheses of mesoporous materials, Microporous Mesoporous Mater. 125 (3) (2009) 170–223.
[38] X. Zhou, L.-J. Wan, Y.-G. Guo, Binding SnO_2 nanocrystals in nitrogen-doped graphene sheets as anode materials for lithium-ion batteries, Adv. Mater. 25 (15) (2013) 2152–2157.
[39] B. Jiang, Y. He, B. Li, S. Zhao, S. Wang, Y.-B. He, et al., Polymer-templated formation of polydopamine-coated SnO_2 nanocrystals: anodes for cyclable lithium-ion batteries, Angew. Chem. Int. Ed. 56 (7) (2017) 1869–1872.
[40] Z. Chen, M. Zhou, Y. Cao, X. Ai, H. Yang, J. Liu, In situ generation of few-layer graphene coatings on SnO_2-SiC core-shell nanoparticles for high-performance lithium-ion storage, Adv. Energy Mater. 2 (1) (2012) 95–102.
[41] A. Nie, Y. Cheng, S. Ning, T. Foroozan, P. Yasaei, W. Li, et al., Selective ionic transport pathways in phosphorene, Nano Lett. 16 (4) (2016) 2240–2247.
[42] W. Ai, W. Zhou, Z. Du, Y. Chen, Z. Sun, C. Wu, et al., Nitrogen and phosphorus codoped hierarchically porous carbon as an efficient sulfur host for Li-S batteries, Energy Storage Mater. 6 (2017) 112–118.
[43] C.-M. Wang, W. Xu, J. Liu, J.-G. Zhang, L.V. Saraf, B.W. Arey, et al., In situ transmission electron microscopy observation of microstructure and phase evolution in a SnO_2 nanowire during lithium intercalation, Nano Lett. 11 (5) (2011) 1874–1880.
[44] A. Nie, L.-Y. Gan, Y. Cheng, H. Asayesh-Ardakani, Q. Li, C. Dong, et al., Atomic-scale observation of lithiation reaction front in nanoscale SnO_2 materials, ACS Nano 7 (7) (2013) 6203–6211.